Precipitation behavior and properties of Al–50Si–0.5X (*X* = Sc, La, Nb) alloys

Jing Luo[1,2], Richu Wang[1,2], Chaoqun Peng[1,2], Zhiyong Cai[1,2,*] , Yan Feng[1,2], and Xiaofeng Wang[1,2]

[1] School of Materials Science and Engineering, Central South University, Changsha 410083, China
[2] Key Laboratory of Electronic Packaging and Advanced Functional Materials, Hunan Province, Changsha 410083, Hunan, China

ABSTRACT

Microstructure, mechanical, and thermo-physical properties of Al–50Si–0.5X alloys prepared by gas atomization and hot pressing were investigated. The results show that the introduction of 0.5% alloying elements has little effect on the size, distribution, and morphology of Si phase as compared with that of the Al–Si alloys. By adding Sc, La, and Nb, the precipitates in the alloys identified by electron probe microanalysis (EPMA) and energy-dispersive spectrometer of the transmission electron microscope (TEM-EDS) are $AlSi_2Sc_2$, Al_2Si_2La, and $NbSi_2$, respectively. The Brinell hardness, tensile strength, and flexural strength of the alloys are improved, which is attributed to the formation of fine precipitates with a volume fraction of 2.5–3.6%. However, the fracture toughness and impact toughness decrease with the addition of alloying elements. The contribution of precipitates on strength can be well explained by the precipitation strengthening mechanism. Furthermore, the thermal conductivity (135.3–136.8 $W \cdot m^{-1} \cdot K^{-1}$) and coefficient of thermal expansion (13.5×10^{-6}/K–13.8×10^{-6}/K) of the alloys were measured, which meet the requirements of electronic packaging materials.

1 Introduction

Nowadays, electronic packaging technology is developing rapidly towards miniaturization. The power density increases gradually as the size of the device decreases. The development and application of advanced electronic packaging materials (EPMs) have become an urgent problem [1]. EPMs are not only the heat dissipation channel of device, but also play a supporting and sealing protection role. To ensure high reliability, EPMs require excellent strength in addition to high thermal conductivity and low coefficient of thermal expansion (CTE).

Among the EPMs, Al-high Si alloys have excellent comprehensive performance, such as high thermal conductivity, adapted CTE, low density, and easy surface coating and laser welding [2, 3]. With the increase of Si content, the alloy strength is improved and the CTE is reduced. These characteristics make Al-high Si alloys considered an ideal candidate in the

Address correspondence to E-mail: zycaimse@163.com

field of thermal management and EPMs. In recent years, the research and application of Al-high Si alloys have made great progress, but there are still some problems, such as low strength and easy cracking during laser welding.

Generally, the alloy strength can be improved by grain size refinement strengthening, precipitation strengthening, solution strengthening, and work hardening strengthening. Due to the intrinsic brittleness of Si, the strength of Al-high Si alloys cannot be improved by plastic deformation, but the alloys can be strengthened by changing the preparation method to refine the grains or adding alloying elements to precipitate the secondary phases.

There are many methods to prepare Al-high Si alloys such as semi-solid forming [1], melt infiltration [4], rapid solidification/powder metallurgy [5], spray deposition [3], and the recently developed selective laser melting [6]. The Al-high Si alloy prepared by rapid solidification had noticeable grain refinement and high preparation efficiency, which can be used in mass production [5]. Li et al. [7] reported that the size of Si phase in spray-deposited Al–45Si alloy was smaller than that prepared by liquid–solid separation, resulting in higher mechanical properties. Compared with the as-cast alloys, primary Si phase in the spray-deposited Al–xSi (x = 18, 25, 35, and 50) alloys was refined obviously, and their size was less than 5 μm, 5 μm, 10 μm, and 12.5 μm, respectively [3, 8]. However, internal holes are commonly observed in the spray deposited bullet, which need further densification. The relative densities of rapid solidified/hot-pressed Al–xSi (x = 55, 70, and 90) alloys were above 99%, which meets the requirements of EPMs [9]. Similarly, Cai et al. [5] studied the Al–(22–50) Si alloys and found that strength and Brinell hardness of the alloys were improved significantly with the increase of Si content.

Mg and Cu are commonly used as alloying elements in the traditional Al alloys due to their high solid solution at high temperature and low solid solubility at ambient temperature. Compared with the Al–50Si alloy, tensile strength of the Al–50Si–1X (Cu or Mg) alloys was enhanced by 27.2% and 24.5%, respectively [10, 11]. The improved strength was attributed to the formation of Al_2Cu or Mg_2Si. However, the microstructure uniformity of Al–50Si alloys decreased gradually when the Cu or Mg content exceeds 2%, leading to the decrease of tensile strength. Many researchers turned their attentions to

the addition of rare earth elements to Al–Si alloys, such as Sc, Y, La, Ce, and Yb. Adding rare earth elements in the cast Al–Si alloy can refine α-Al grains, reduce the secondary dendrite arm spacing (SDAS), and modify the morphology of the eutectic Si, and finally improve the alloy strength. Sc and La are considered as a multi-refinement modifier. Xu et al. [12] reported that Sc has multiple modification effects on the microstructure of Al–Si–Mg alloy, such as refining grain, reducing secondary dendrite arm spacing, modifying eutectic Si, and transforming harmful iron-bearing phase. Tzeng et al. [13] found that the addition of 0.1% Sc transformed the acicular β-Al_5FeSi phase into a Chinese-Script phase in the as-cast Al–11.6Si alloy, which led to the improved ultimate tensile strength (UTS) and hardness. The addition of 0.1% La not only refined α-Al grain of Al–7Si alloy, but also formed La-rich phase (Al_2Si_2La), which hindered the growth of eutectic Si [14]. Although Nb is not a rare earth element, it has similar effect as rare earth elements on cast Al–Si alloys. This phenomenon is attributed to the formation of stable Nb-based intermetallic compound, and the crystal grain is refined. Thus, Nb is also considered to be a very promising candidate alloying element [15, 16]. At present, there are few reports on effect of alloying elements on microstructure and properties of Al-high Si alloys prepared by gas atomization and hot pressing. Due to the presence of large primary Si in Al-high Si alloys, alloying elements have little effect on the refinement and modification of Si phase. But the alloying elements form second phases in the matrix and improve the alloy strength. Kilicaslan et al. [17] studied the effect of adding 0.6% Sc on the microstructure and mechanical properties of Al–20Si alloy at as-atomized and extruded state. The size of primary Si and eutectic Si decreased slightly when 0.6% Sc was added, and the ultimate tensile strength increased from 200 to 370 MPa. The Si phase in the spray deposited Al–(13–22) Si–0.8Sc alloys was refined, and the average size was only 5–10 μm [18]. When compared with the binary Al–Si alloys, the $AlSi_2Sc_2$ precipitated in the matrix and improved the strength of alloys containing Sc. Moreover, when alloying elements are added to enhance the mechanical properties, the thermal–physical properties of the alloy should also meet the requirements of electronic packaging materials. Therefore, the weight percentage of alloying elements in Al-high Si alloys is generally controlled to be up to 0.5 wt%.

In this paper, Al–50Si–0.5X (X = Sc, La, and Nb) alloys were prepared by gas atomization and hot pressing. The effects of alloying elements on the microstructure and properties of Al–50Si–0.5X (X = Sc, La, and Nb) were investigated. Emphasis was paid on the comparison and analysis of precipitation behavior in the alloys containing alloying elements. The volume fraction of precipitates on strength, thermal conductivity, and CTE of the alloys was discussed.

2 Experimental process

2.1 Materials preparation

The raw materials are pure Al (purity ≥ 99.95%), pure Si (purity ≥ 99.0%), and Al–2Sc, Al–10La, and Al–10Nb materials (all components in this paper refer to weight percentages). Al–50Si–0.5X (X = Sc, La, and Nb) alloy powders were prepared by gas atomization using N_2. Details of melting and gas atomization process were reported in the previous papers [5, 10]. First, the alloy powder with particle size less than 74 μm was selected, and cold pressed at 400 MPa for 2 min. Compacts with relative densities of 75–83% were obtained. Second, the compacts were hot-pressed at 560 °C for 60 min. In the process of hot pressing, the maximum holding pressure was 45 MPa. After sintering, the samples were cooled to below 200 °C and then the pressure was relieved. The samples were cooled to room temperature in the furnace. Finally, Al–50Si–0.5X alloys with the dimension of 60 mm × 20 mm × 100 mm were obtained. Chemical compositions of the Al–50Si–0.5X alloys measured by ICP-AES are listed in Table 1.

2.2 Microstructure characterization

The performance test specimens of Al–50Si–0.5X alloys were cut by wire electro-discharge machining (WEDM) and machined. Morphology of Si phase was observed using optical microscope (LEICA DM4M). Microstructure and tensile fracture surface of the alloys were observed using Quanta-200 environmental scanning electron microscope (SEM, Quanta 200). The specimens for microstructural observation were ground, polished, and etched with Keller's reagent for 30 s at room temperature. Size and volume fraction of the precipitates were counted using the Image-Pro Plus (IPP) software. To ensure the representative of the statistical data, ten images of each alloy were randomly selected from the SEM result at the same magnification. The qualitative analysis of precipitates was conducted using transmission electron microscopy (TEM, FEI Talos F200X). The scanning angle range of 2θ was 20°–80° and the scanning speed was 2 (°)/min. The TEM specimens were mechanically polished to 50 μm and thinned to perforations using a Gatan 691 ion thinner. An electron probe microscopic analyzer (JXA-8230 electron probe microanalyzer) was employed to determine the distribution of alloying elements.

2.3 Performance testing

Density of the Al–50Si–0.5X alloys was determined by Archimedes drainage method. The mass of the alloy was measured using an electronic scale. Brinell hardness of the alloys was measured using an HBS-3000B Brinell hardness tester, and the result was an average of five tests. The load was set to 187.5 kgf, the dwell time was 34 s, and the diameter of steel ball was 2.5 mm.

The tensile and compressive properties were tested by an MTS 850 fatigue testing machine at a constant strain rate of 0.5 mm/min. Dog bone-shaped specimens with a gauge diameter of 6 mm and gauge length of 35 mm were used for the tensile test. The specimens for the compressive test were Φ10 mm × 30 mm. The flexural strength was tested using an MTS 858 fatigue testing machine at a constant strain rate of 0.1 mm/min. The specimens for the bending test were 50 mm × 10 mm × 5 mm. The Al–50Si alloy is quite brittle compared with traditional Al alloys. The impact toughness test was conducted on the unnotched specimen, and the fracture toughness

Table 1 Chemical composition of the Al–50Si–0.5X alloys (wt%)

Alloy	Si	Sc	La	Nb	Others	Al
Al–50Si	50.2	–	–	–	< 0.01	Bal
Al–50Si–0.5Sc	50.4	0.53	–	–	< 0.01	Bal
Al–50Si–0.5La	49.8	–	0.51	–	< 0.01	Bal
Al–50Si–0.5Nb	50.4	–	–	0.48	< 0.01	Bal

test was conducted on the K_{Ic} dense tensile specimen. According to ASTM-E399, the dimension of the fracture toughness specimen is 40 mm wide and 20 mm thick with a 2 mm prefabricated crack, as shown in Fig. 1. Three parallel specimens were used for the mechanical tests.

Under the argon atmosphere, CTE of the four alloys in the range of 100–500 °C was measured by using thermo-mechanical tester (NETZSCH DIL 402PC, Germany). The thermal diffusivity and specific heat of the alloys were measured by laser flash and calorimetric method (NETZSCH LFA427/3/G, Germany). Thermal conductivity of the alloys was calculated by thermal diffusivity and specific heat. The dimensions of CTE and thermal conductivity specimens were 20 mm × 5 mm × 5 mm and Φ10 mm × 3 mm, respectively. Each component was tested three times.

3 Results

3.1 Microstructural characteristics

The relative densities of the Al–50Si–0.5X (X = Sc, La, Nb) alloys are higher than 99.8%, indicating that the atomized alloy powders were well densified by hot pressing. Fine and homogenous microstructures of the four alloys were obtained, as shown in Fig. 2. It is seen that the Si phase is connected in bluish-gray bulge. There is no significant difference concerning the size, distribution, and morphology of Si phase among the Al–50Si alloys without and with adding different alloying elements. There is a white and continuous Al matrix between the Si phase, which provides a channel for the heat conduction of the

alloys. Due to the low solid solubility of Si in Al at room temperature, the Al matrix could be considered as pure Al. The precipitates in the alloys containing Sc, La, and Nb are too small to be observed by optical microscope.

The SEM image of the Al–50Si alloy is shown in Fig. 3a. The relatively dark and raised area is the Si phase, whereas the lighter and flat surface is the Al matrix. The inter-connected Si phase can be clearly observed. No secondary phase or fine Si phase was observed in the alloy. Figure 3b–d shows the microstructures of Al–50Si alloys containing 0.5%Sc, 0.5%La, and 0.5%Nb, respectively. Fine and white precipitates dispersed in the matrix were observed. There is no significant difference in the size and distribution of precipitates in these alloys at this magnification. However, the distribution of Si phase in the Al–50Si–0.5X alloys seems to be different from that in the Al–50Si alloy, as compared with Fig. 3b–d and Fig. 3a.

According to the refs. [19, 20], adding Sc and La to Al–Si alloys will form $AlSi_2Sc_2$ (V phase) or Al_3Sc and Al_xSi_xLa precipitates, respectively. As the ternary phase is unstable at low temperature, the secondary phase in Al–Si–Nb alloy is likely to exist as a binary phase, such as Nb_5Si_3, $NbAl_3$, and $NbSi_2$ [21, 22]. To determine the precipitates in Al–50Si–0.5X alloys, XRD measurements were carried out and the XRD patterns are depicted in Fig. 4. The diffraction peaks of secondary phases are not clearly observed due to the low content of alloying elements.

The EPMA maps of the Al–50Si–0.5X (X = Sc, La, Nb) alloys showing the distribution of elements are exhibited in Fig. 5. The Si phase is light gray, the Al matrix is dark gray, and the precipitates are irregular white particles. The change of color from red to blue

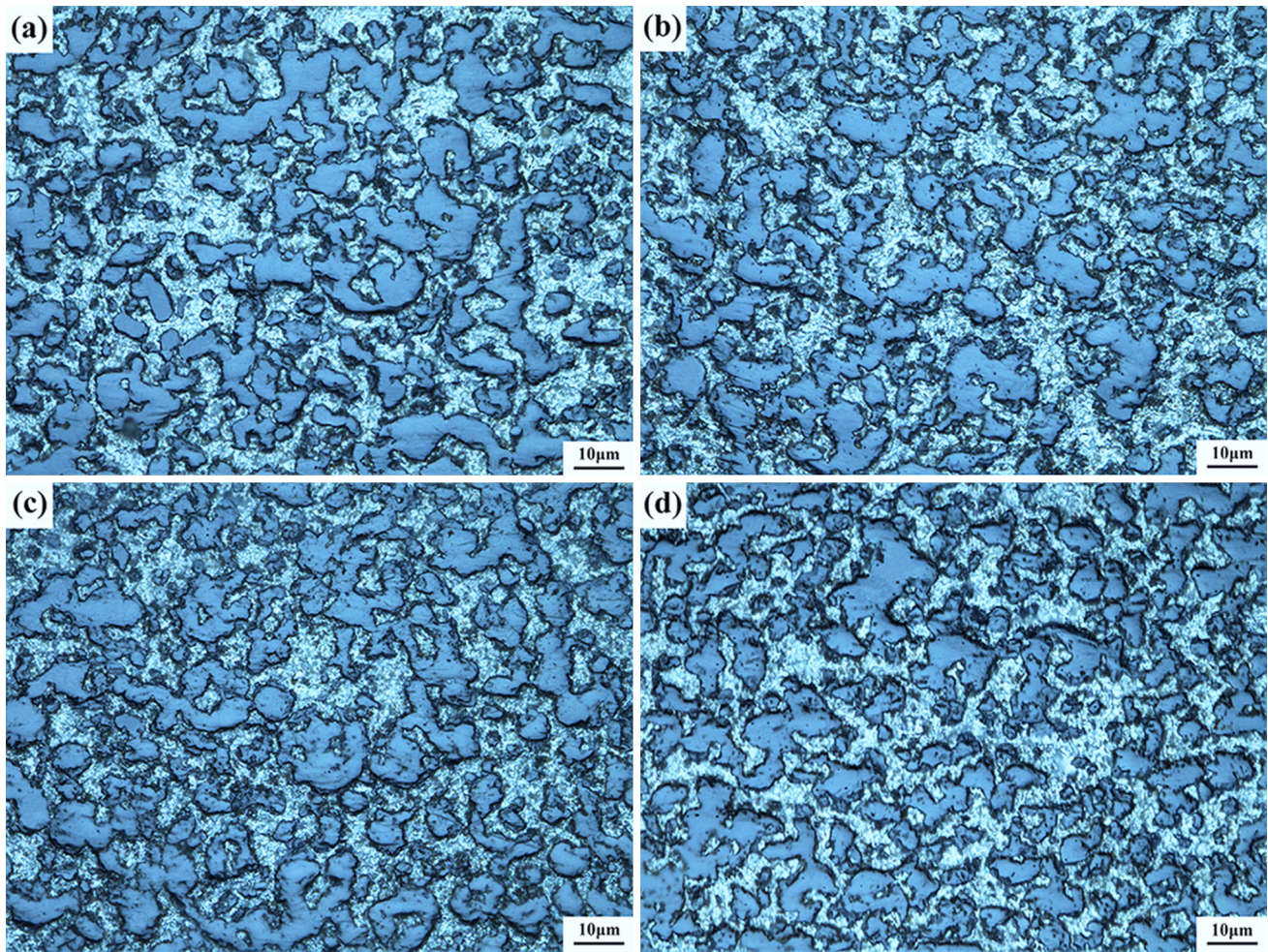**Fig. 1** Dimension of fracture toughness specimen
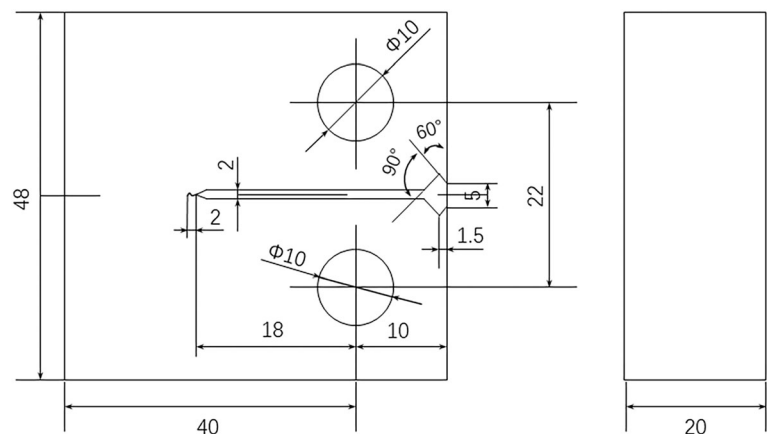
Fig. 2 Optical micrographs of the **a** Al–50Si, **b** Al–50Si–0.5Sc, **c** Al–50Si–0.5La, and **d** Al–50Si–0.5Nb alloys

represents the change of concentration element content from high to low. In the three alloys, the distributions of Al and Si elements are quite uniform without obvious difference. However, the alloying elements are enriched in the precipitates. Additionally, the area distributions of the three alloying elements are quite different, which is related to the compound formed during gas atomization and hot pressing.

Figure 6 displays TEM bright-field images of the precipitates along $<110>_{Al}$ zone axis in the Al–50Si–0.5X (X = Sc, La, Nb) alloys. At the orientation of $<110>$, the morphology of the precipitates is short rod-like and dot-like. Figure 7 shows the distribution of elements under high-angle annular dark-field scanning transmission electron microscopy (HAADF-STEM) and TEM-EDS. The alloying

elements are enriched in the precipitates in the Al–50Si–0.5X (X = Sc, La, Nb) alloys. The precipitates in the Al–50Si–0.5X alloys were analyzed by TEM-EDS, and they are determined as $AlSi_2Sc_2$, Al_2Si_2La, and $NbSi_2$, respectively. The chemical compositions of each precipitate in Fig. 7 represent the average value of different particles in the same field. In the ternary phase diagram of Al–Si–Sc, only one ternary compound, $AlSi_2Sc_2$ (V phase), has been observed at ternary eutectic reaction at 575.3 °C [23]. The phase is considered thermodynamically stable. According to Fig. 7b, the atomic ratio of the La-rich phase is close to 2:2:1 (Al: Si: La), that is the Al_2Si_2La phase. The size of the precipitates agrees with the SEM images. Due to the instability of $Al_2Si_5Nb_3$ ternary phase at low temperature, the precipitate in the Al–50Si–0.5Nb alloy is the $NbSi_2$ binary phase.
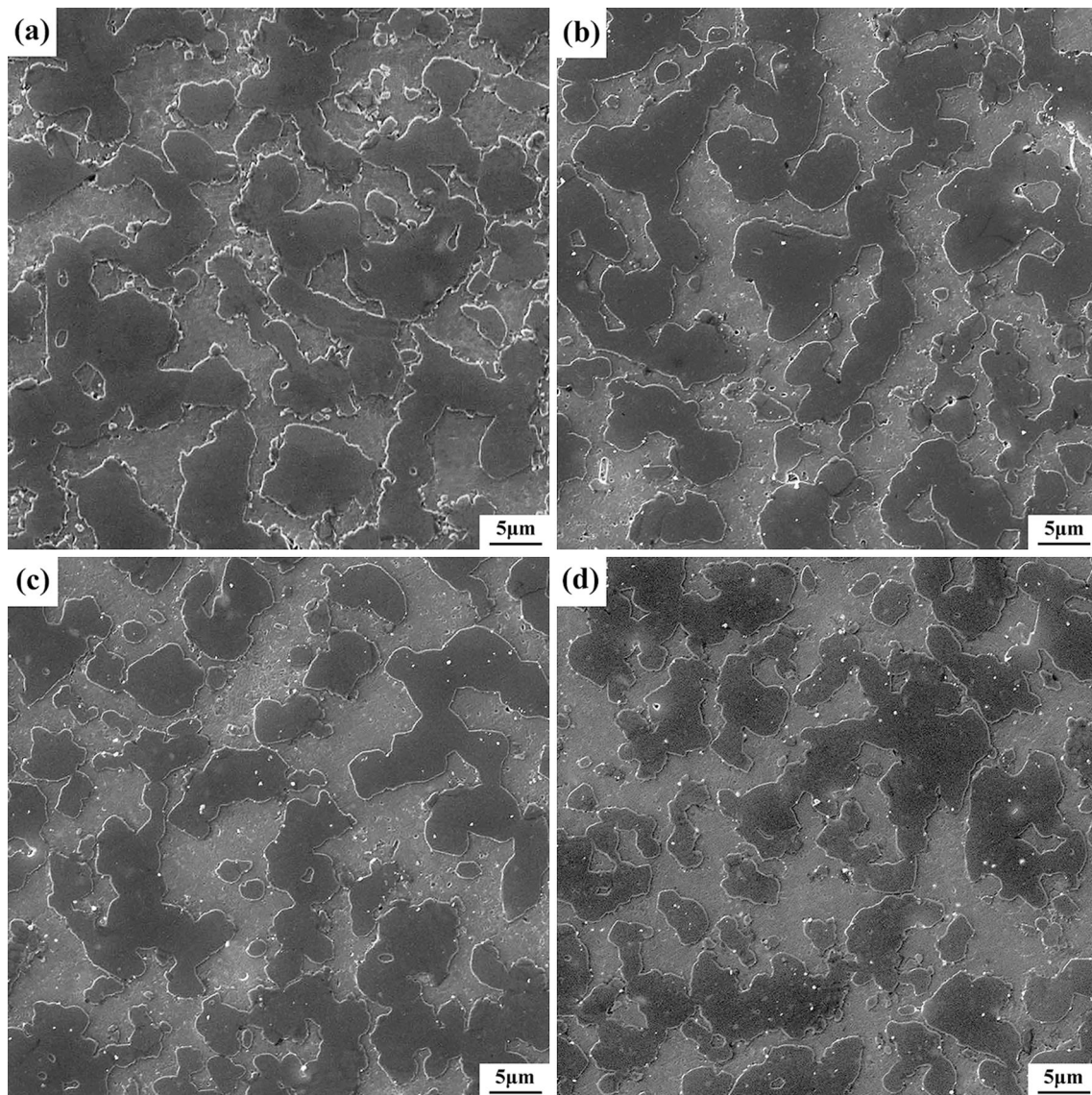
Fig. 3 SEM microstructures of the **a** Al–50Si, **b** Al–50Si–0.5Sc, **c** Al–50Si–0.5La, and **d** Al–50Si–0.5Nb alloys

3.2 Mechanical properties

The tensile strength, compressive strength, flexural strength, and Brinell hardness of the Al–50Si–0.5X (X = Sc, La, Nb) alloys are listed in Table 2. Since the hard and brittle nature of Si phase, the Brinell hardness is measured. The Brinell hardness of the Al–50Si alloy is 137.6 HB, and that of the alloys containing 0.5%Sc, 0.5%La, and 0.5%Nb increase to143.4 HB, 153.9 HB, and 162.6 HB, respectively.

Compared with the Al–50Si alloy, the ultimate tensile strength of the Al–50Si–0.5X alloys increases by 10.0%, 14.7%, and 19.4%, respectively, and the elongation decreases from 0.4 to 0.1% accordingly.

The tensile stress–strain curves of the Al–50Si–0.5X alloys at room temperature are illustrated in Fig. 8. There is no yield point in the curves. According to the stress–strain curves and elongation results, the Al–50Si–0.5X alloys exhibit obvious brittle fracture.

Then, the three-point flexural performance tests were carried out. Compared with the Al–50Si alloy, the flexural strength of the alloys containing Sc, La, and Nb increase by 2.6%, 6.5%, and 11.7%, respectively. The result is consistent with the value of tensile strength.

Additionally, the compressive performance of the Al–50Si–0.5X alloys was also measured. The results
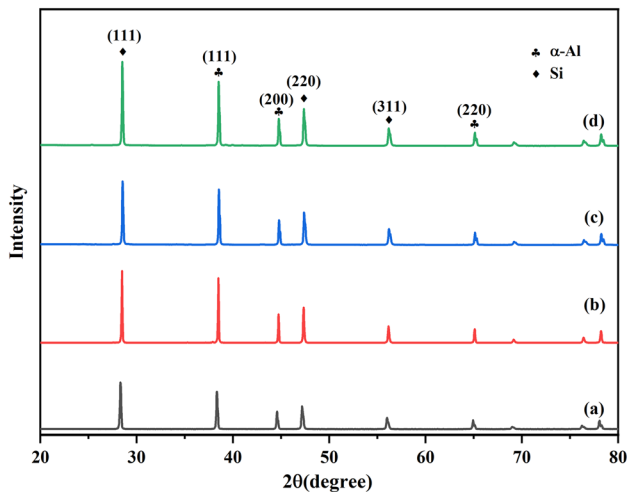
Fig. 4 XRD patterns of the **a** Al–50Si, **b** Al–50Si–0.5Sc, **c** Al–50Si–0.5La, and **d** Al–50Si–0.5Nb alloys

show that the alloying elements have a negligible effect on the compressive strength of the alloys.

Fracture toughness is one of the important mechanical properties, but there are few reports on fracture toughness of Al-high Si alloys. The fracture toughness of the Al–50Si–0.5X (X = Sc, La, Nb) alloys were measured to be 4.4–4.7 MPa.m$^{1/2}$ in Table 3. The fracture toughness of Si and pure Al is approximately 0.6 MPa.m$^{1/2}$ and 25.6 MPa.m$^{1/2}$, respectively [24]. Although the content of Si has little difference among the alloys, their fracture toughness is equivalent to that of the Al-65Si alloy prepared by powder metallurgy (K_{Ic} 4.56 MPa.m$^{1/2}$ [25]).

Impact toughness reflects the ability of material to resist the impact load. Impact toughness refers to the ability of a material to absorb plastic deformation work and fracture work under impact load, reflecting the subtle defects and impact resistance of the material. Therefore, the impact strength can be used as an assessment of the resistance of an alloy under fast loading conditions. The Al–50Si–0.5X (X = Sc, La, Nb) alloys are brittle, and their unnotched specimens are more accurate than U-notched and V-notched specimens. According to the literatures, the unnotched impact toughness of cast hypoeutectic 356 and 319 alloys are 6.4×10^4 J.m^{-2} and 4.06×10^4 J.m^{-2}, respectively [26, 27]. In this work, due to the rapid solidification process of gas atomization, the impact toughness of Al–50Si alloy is up to 1.4×10^4 J.m^{-2}. However, the impact toughness of the Al–50Si–0.5X alloys was slightly reduced compared with the Al–50Si alloy, as listed in Table 3.

Figure 9 shows the tensile fracture morphology of the Al–50Si–0.5X (X = Sc, La, Nb) alloys. The surfaces exhibit transgranular type brittle features and few signs of ductile fracture. The overall morphologies of fracture surface indicate that the addition of alloying elements have little impact on the fracture behavior of the Al–50Si–0.5X alloys, as shown in Fig. 9a–d. Cracks propagate from the surface to the interior of the tensile sample with the increase of tensile stress, indicating that there are no defects such as holes in the alloys. The fracture surface of the alloys is flush with no fiber area and shear lip, but the radiation area is clearly observed. The alloys containing alloying elements exhibit more obvious brittle fracture features in accordance with the tensile stress–strain curves in Fig. 8. There is no apparent plastic deformation before fracture and the macroscopic fracture mechanism is a positive fracture.

It can be seen from the magnified images in Fig. 9e–h that the cracks first form at the Si phase, then pass through the Al matrix and form a small number of dimples. The Si phase fails in brittle fracture mode while the Al matrix fails in ductile fracture. Cracks usually propagate along with the brittle Si and precipitates. Low-strength and brittle Si phase acts as the crack source. The fracture behavior of the Al–50Si alloys can be confirmed by the three-point bending crack path in Fig. 10. Moreover, no interface debonding between the Si phase and Al matrix is observed, which is attributed to the solid solubility of Si in Al matrix. Additionally, the pre-alloyed powder can also improve the bonding strength between Si phase and Al matrix.

3.3 Thermo-physical properties

Table 4 lists the thermal conductivity and CTE of the Al–50Si–0.5X (X = Sc, La, Nb) alloys. The thermal conductivity of the alloys is reduced after the addition of alloying elements. The Al–50Si–0.5Nb alloy has the lowest value of 135.3 W·m^{-1}·K^{-1}, which is 2.9% lower compared with that of the Al–50Si alloy. However, this also meets the thermal conductivity requirements of electronic packaging, above 120 W·m^{-1}·K^{-1}. Heat conduction in solids depends mainly on the movement of free electrons and phonons in the Al–50Si–0.5X (X = Sc, La, Nb) alloys. While the thermal conductivity is the result of the combined action of both phonons and free electrons movement. The Al–50Si alloys with different alloying
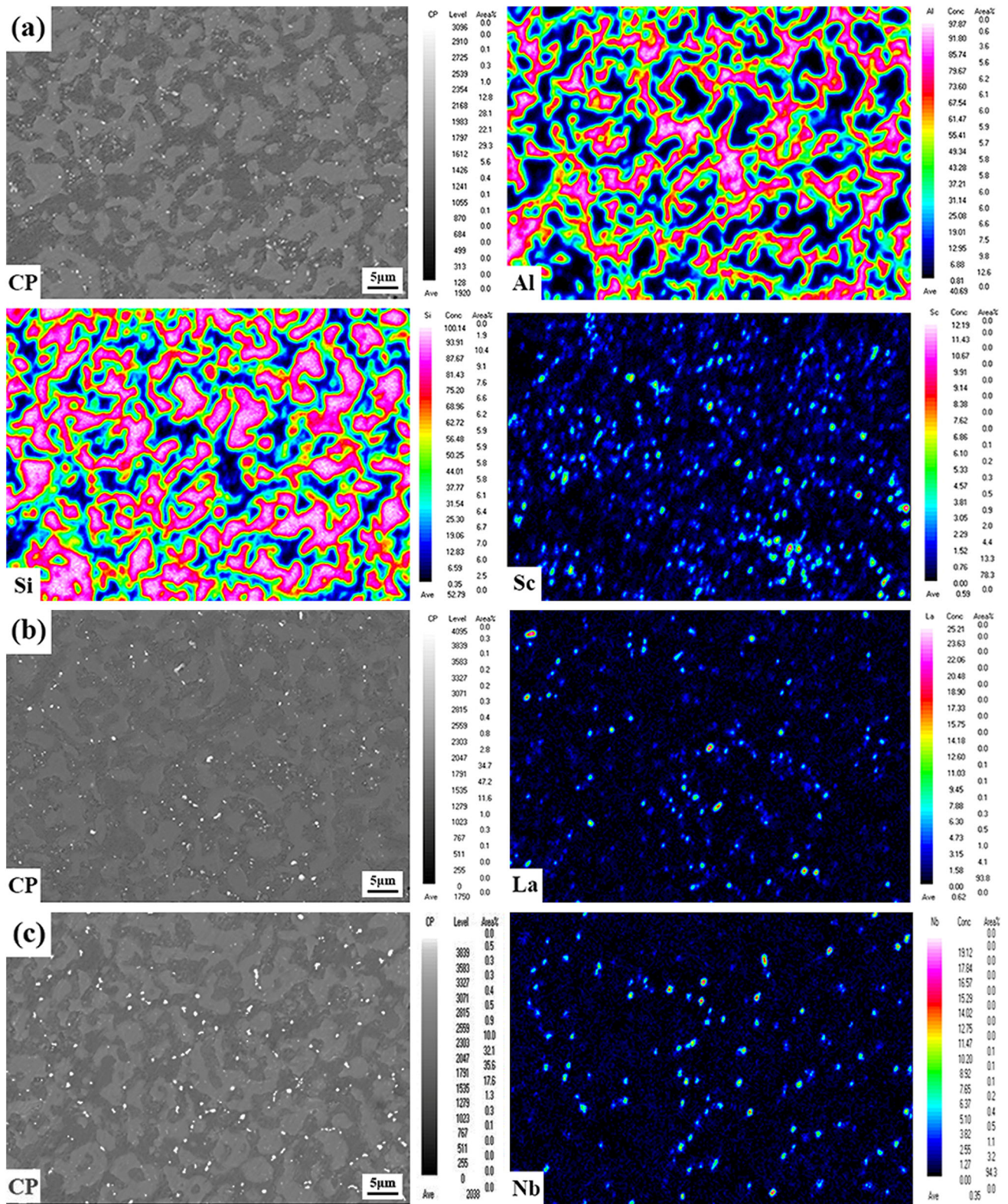
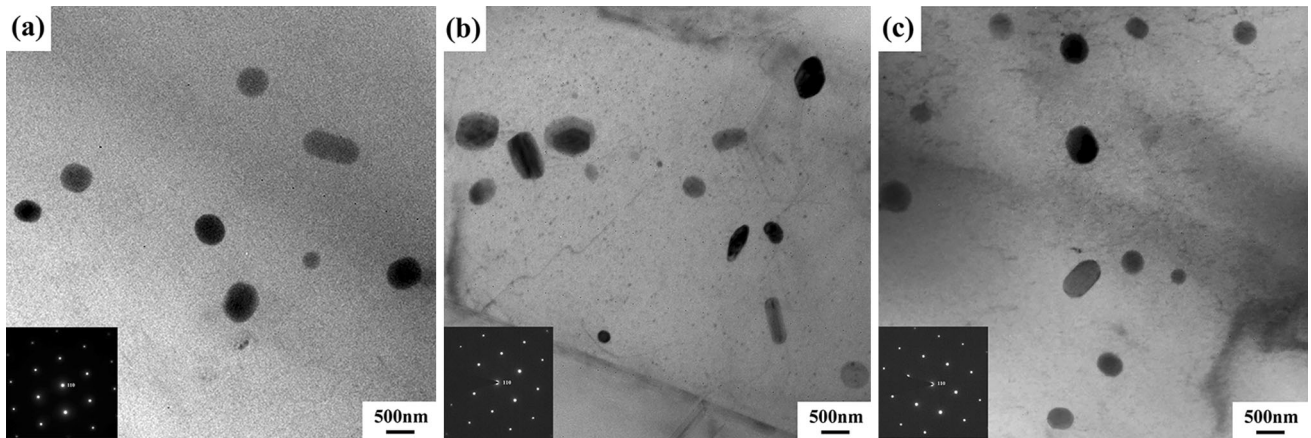**Fig. 5** EPMA maps of the **a** Al–50Si–0.5Sc, **b** Al–50Si–0.5La, and **c** Al–50Si–0.5Nb alloys

Fig. 6 TEM images of the **a** Al–50Si–0.5Sc, **b** Al–50Si–0.5La, and **c** Al–50Si–0.5Nb alloys
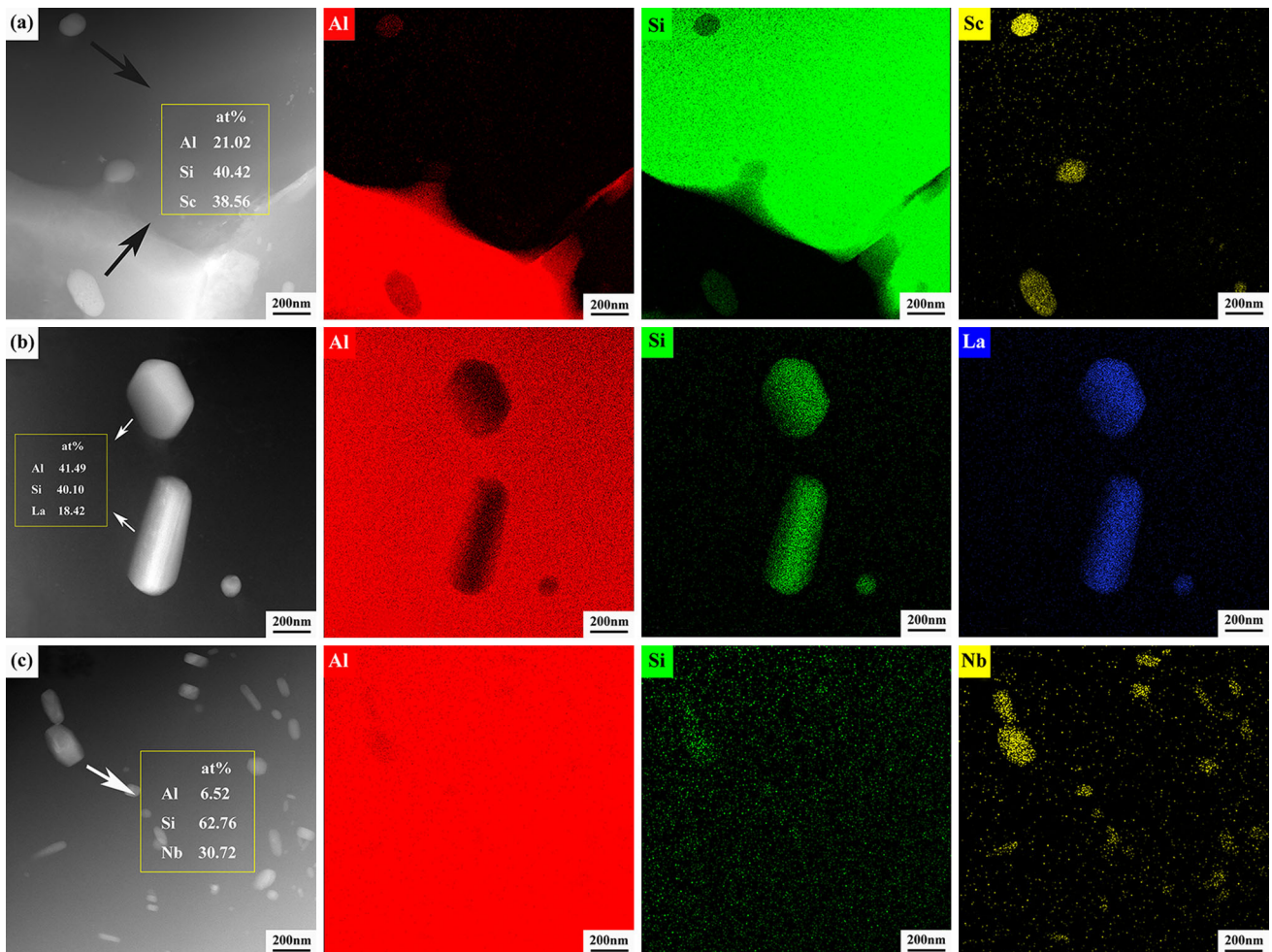

Fig. 7 HAADF-STEM images and EDS elemental mappings of the **a** Al–50Si–0.5Sc, **b** Al–50Si–0.5La, and **c** Al–50Si–0.5Nb alloys

elements have different types of precipitates. The appearance of precipitates increases the interface area of two phases in the alloy. The interface has a scattering effect on the movement of phonons and free electrons, resulting in the lower thermal conductivity. Additionally, the CTE of the precipitates does not match the matrix, and the interface stress field is also

Table 2 Mechanical properties of the Al–50Si–0.5X (X = Sc, La, Nb) alloys

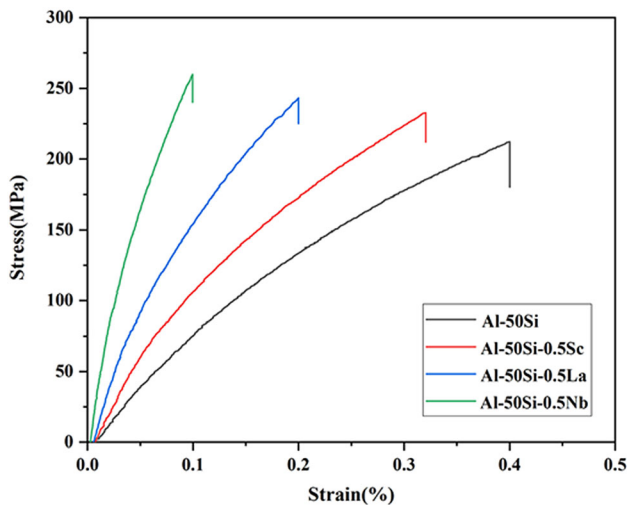| Material	Brinell hardness (HB)	Tensile strength (MPa)	Elasticity modulus (GPa)	Flexural strength (MPa)	Compressive strength (MPa)
Al–50Si	137.6 ± 1.1	212.7 ± 4.0	103.3 ± 0.8	301.8 ± 4.5	440.0 ± 3.3
Al–50Si–0.5Sc	143.4 ± 1.5	234.0 ± 4.4	105.2 ± 0.5	309.6 ± 5.6	441.0 ± 2.5
Al–50Si–0.5La	153.9 ± 2.8	244.0 ± 4.6	106.5 ± 0.5	321.5 ± 4.8	449.0 ± 3.6
Al–50Si–0.5Nb	162.5 ± 1.0	254.0 ± 3.0	108.1 ± 0.4	337.2 ± 4.5	453.0 ± 3.3

Fig. 8 Tensile stress–strain curves of the Al–50Si–0.5X (X = Sc, La, Nb) alloys

detrimental to the thermal conductivity to some extent.

The variation of CTE of the alloys in the range from 100 °C to 500 °C is shown in Fig. 11. The CTE increases gradually with the increase of temperature, and all curves have similar trends. Furthermore, the CTE increases rapidly at first and then tends to be relatively flat. Among the three alloys, the CTE of the Al–50Si–0.5Nb alloy is the smallest, followed by the Al–50Si–0.5La alloy and Al–50Si–0.5Sc alloy. The decrease of CTE is attributed to the formation of precipitates, which forms many interfaces in the alloys and impedes the thermal expansion of Al matrix. The thermal expansion of the alloys is due to the combined effect of the Al matrix, Si phase, and precipitates. The Al matrix does not undergo plastic deformation at low temperature, so the CTE increases linearly with the increase of temperature. With the increase of temperature, the yield strength of Al matrix decreases, but the interfacial thermal stress in the alloys increases gradually. At high temperature, when the thermal stress exceeds the yield strength of the Al matrix, plastic deformation occurs in the matrix, which offsets part of the thermal expansion of the Al matrix. Therefore, the CTE of Al–50Si alloys increases slowly at high temperature.

4 Discussion

4.1 Precipitates formation in the Al–50Si–0.5X alloys

It can be seen from the above results that the densities of gas-atomized/hot-pressed Al–50Si–0.5X (X = Sc, La, Nb) alloys are as high as 99.8%, indicating that the defects such as original particle interface and pores in the samples are well eliminated.

The precipitates in the Al–50Si–0.5Sc alloy could be Al_3Sc and $AlSi_2Sc_2$ (V phase). It is reported that the formation of Al_3Sc phase was inhibited by adding more than 0.1% Si in the Al–Sc binary alloy [18]. The precipitate in the Al–50Si–0.5Sc alloy is confirmed to be $AlSi_2Sc_2$ (V phase) by the TEM-EDS. The $AlSi_2Sc_2$

Table 3 Toughness properties of the Al–50Si–0.5X (X = Sc, La, Nb) alloys

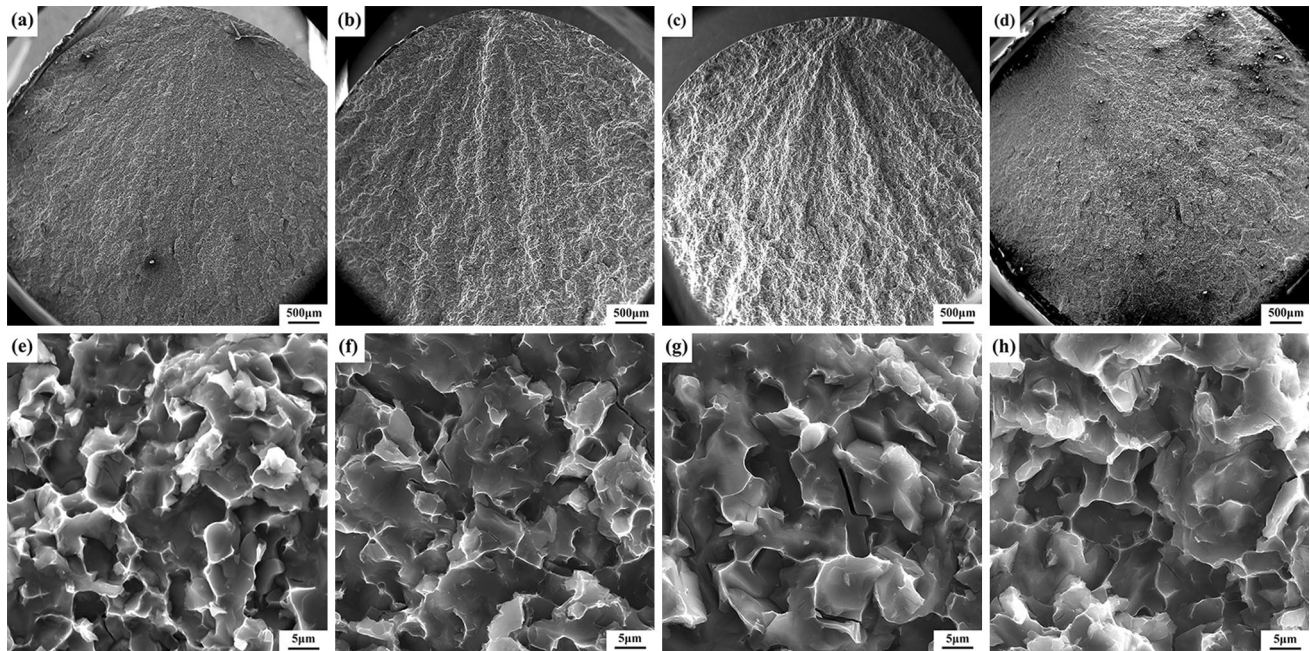| Material	Fracture toughness (K_{Ic}) (MPa.m$^{1/2}$)	Impact toughness (ak) ($\times 10^4$ J.m^{-2})
Al–50Si	4.7 ± 0.2	1.4 ± 0.2
Al–50Si–0.5Sc	4.6 ± 0.4	1.3 ± 0.1
Al–50Si–0.5La	4.5 ± 0.3	1.3 ± 0.2
Al–50Si–0.5Nb	4.4 ± 0.2	1.2 ± 0.1

Fig. 9 Tensile fractography of the **a, e** Al–50Si, **b, f** Al–50Si–0.5Sc, **c, g** Al–50Si–0.5La, and **d, h** Al–50Si–0.5Nb alloys

phase with tetragonal (P4/mbm) is a brittle phase and is more easily formed in thermodynamics than Al_3Sc. Meanwhile, $AlSi_2Sc_2$ phase is also a mechanically stable intermetallic compound [28]. The lattice parameters are $a = b = 6.597$ Å, $c = 3.3994$ Å, and $\alpha = \beta = \gamma = 90°$ (ICSD:52,653).

There are three equilibrium phases in the Al–Si–La system at 500 °C, which are Al_2Si_2La, $AlSi_2La$, and $Al_{1.64-1.85}Si_{0.36-0.15}La$. Elgallad et al. [29] reported that the Al–Si–La phase formed at about 566 °C in A413 alloy and A356 alloy, where the atomic ratio of Al:Si:La is close to 2:2:1. TEM-EDS result of the Al–50Si–0.5La alloy is consistent with the above report. Some researchers reported that Al_2Si_2La had a hexagonal structure $hP5-La_2O_2S$ [30], while others identified it is a hexagonal $hP5-CaLa_2O_2$-type crystal structure [31]. However, the information about Al_2Si_2La is limited, and its crystal structure needs further confirmation.

There are two binary-phase regions (Liquid + $NbAl_3$ and Liquid + $NbSi_2$) and one three-phase region (Liquid + $NbAl_3$ + $NbSi_2$) at the Al-rich corner of the Al–Si–Nb isothermal section at 800 °C [22]. Al_3Nb is stable when Si content is less than 12.0%. However, most of Al_3Nb converts to $NbSi_2$ when the Si content is over 12.9%. Therefore, the precipitates in Al–50Si–0.5Nb alloy are $NbSi_2$ with hexagonal structure and the lattice parameters

are $a = b = 4.819$ Å, $c = 6.592$ Å and $\alpha = \beta = 90°$, $\gamma = 120°$ (ICSD:16,502). The result is consistent with the TEM-EDS results in Fig. 7.

4.2 Precipitation strengthening in the Al–50Si–0.5X alloys

The size and volume fraction of precipitates in the Al–50Si–0.5X (X = Sc, La, Nb) alloys were measured using the Image-Pro Plus (IPP) software. Figure 12 shows the size distribution and volume fraction of the precipitates. The size of the three precipitates is concentrated in the range of 400–600 nm, and the average size is approximately 550.0 nm. The volume fraction of precipitates increases from 2.5 to 3.0% and 3.6% with the addition of Sc, La, and Nb alloying elements sequentially.

As the size of precipitates in the Al–50Si–X (X = Sc, La, Nb) alloys is similar, the alloy strength is highly dependent on the volume fraction of precipitates. The enhanced strength of the alloys is mainly attributed to the precipitation strengthening. There are two methods to explain the precipitation strengthening mechanism, namely, the Orowan looping mechanism and particle cutting mechanism. The interface between precipitates and matrix and the size of precipitates are the basis for judging which mechanism works. Generally, the Orowan looping mechanism
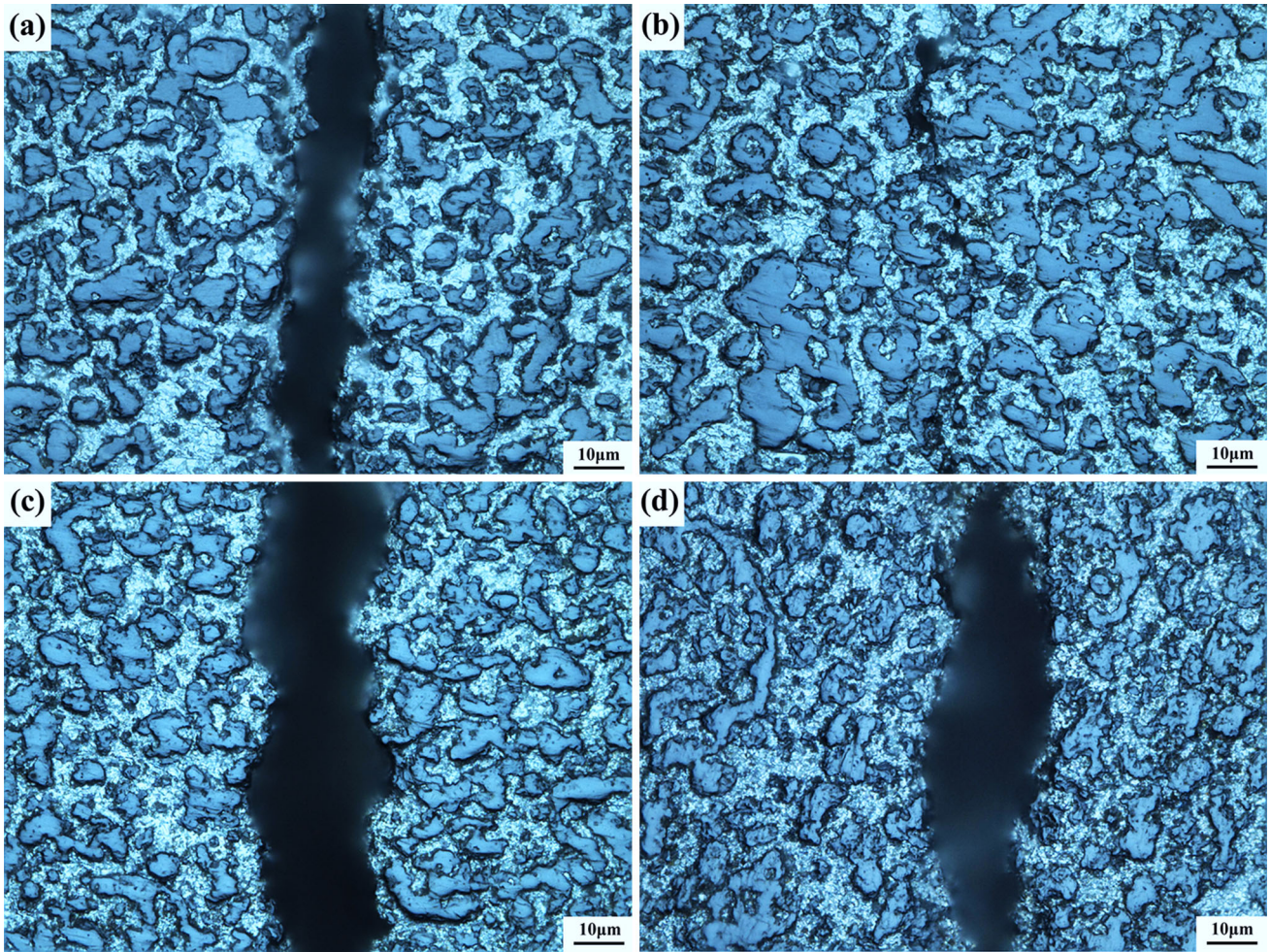
Fig. 10 Bending crack resistance of the **a** Al–50Si, **b** Al–50Si–0.5Sc, **c** Al–50Si–0.5La, and **d** Al–50Si–0.5Nb alloys observed using optical microscope

Table 4 Thermal conductivity and CTE of the Al–50Si–0.5X (X = Sc, La, Nb) alloys

Material	Thermal conductivity ($W{\cdot}m^{-1}{\cdot}K^{-1}$)	Coefficient of thermal expansion, $\times 10^{-6}$/K				
		100 °C	200 °C	300 °C	400 °C	500 °C
Al–50Si	139.3 ± 0.7	13.0 ± 0.1	13.7 ± 0.1	14.0 ± 0.3	14.4 ± 0.1	14.5 ± 0.3
Al–50Si–0.5Sc	136.8 ± 0.8	12.9 ± 0.2	13.5 ± 0.2	13.9 ± 0.2	14.3 ± 0.1	14.4 ± 0.3
Al–50Si–0.5La	135.7 ± 0.1	12.6 ± 0.1	13.3 ± 0.2	13.8 ± 0.1	14.2 ± 0.1	14.4 ± 0.1
Al–50Si–0.5Nb	135.3 ± 1.1	12.4 ± 0.2	13.2 ± 0.1	13.7 ± 0.1	14.1 ± 0.1	14.3 ± 0.2

applies to the non-deformable particles that are incoherent with the matrix, and the particle cutting mechanism applies to the deformable particles that are coherent with the matrix. Figure 13 displays the high-resolution TEM images of the precipitates. The region of lattice distortion between the precipitates and the Al matrix is marked by the white dashed circles. It is seen that there is an extreme mismatch between the precipitates and the Al matrix, indicating that the precipitates are incoherent with the matrix. Meanwhile, the expression of critical radius
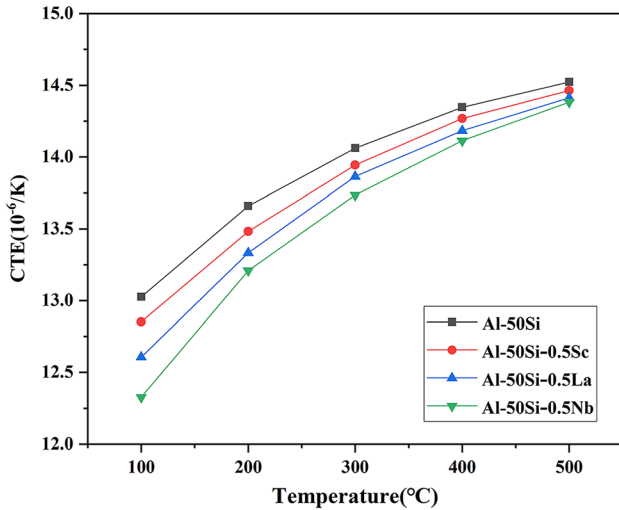
Fig. 11 Coefficient of thermal expansion of the Al–50Si–0.5X (X = Sc, La, Nb) alloys as a function of temperature

of precipitates for the choosing precipitation strengthening mechanism is as follows:

$$r_c = \frac{b}{\delta} \tag{1}$$

$$\delta = (\Delta a_0 / a_0), \tag{2}$$

where b is Burger's vector and δ is the lattice misfit. The exp.2 is a mismatch calculation method proposed

by Turnbull–Vonnegut law and the critical size of precipitates can be calculated [32].

The calculated result indicates that the Orowan looping works when the size of precipitates is larger than 10 nm. The above statistical results show that the size of precipitates is concentrated in 400–600 nm, so the Orowan looping mechanism is the dominant strengthening mechanism in the Al–50Si–0.5X (X = Sc, La, Nb) alloys. The strengthening effect of $AlSi_2Sc_2$, Al_2Si_2La, and $NbSi_2$ precipitates can be calculated by the following formula in the model of Orowan strengthening [33]:

$$\Delta\sigma_{Orowan} = \frac{0.85MGb}{2\pi(1-v)^{1/2}} \frac{\ln(D_p/b)}{\frac{1}{2}D_p\left(\sqrt{\frac{2\pi}{3V_p}} - 2\right)}, \tag{3}$$

where M is the Taylor factor (2.6) [34], G is matrix shear modulus ($G = \frac{E}{2(1+v)}$), v is the Poisson ratio ($v_{Al} = 0.33, v_{Si} = 0.22$), b represents the value of Burger's vector, and D_p and V_p are the size and volume fraction of precipitates, respectively. For the FCC matrix, the value of Burgers vector is $\sqrt{2}a/2$, and the lattice constant of Al is 0.40496 nm. As a result, the contribution of precipitation strengthening in Sc, La, and Nb contained alloys is calculated to be 18.4 MPa,
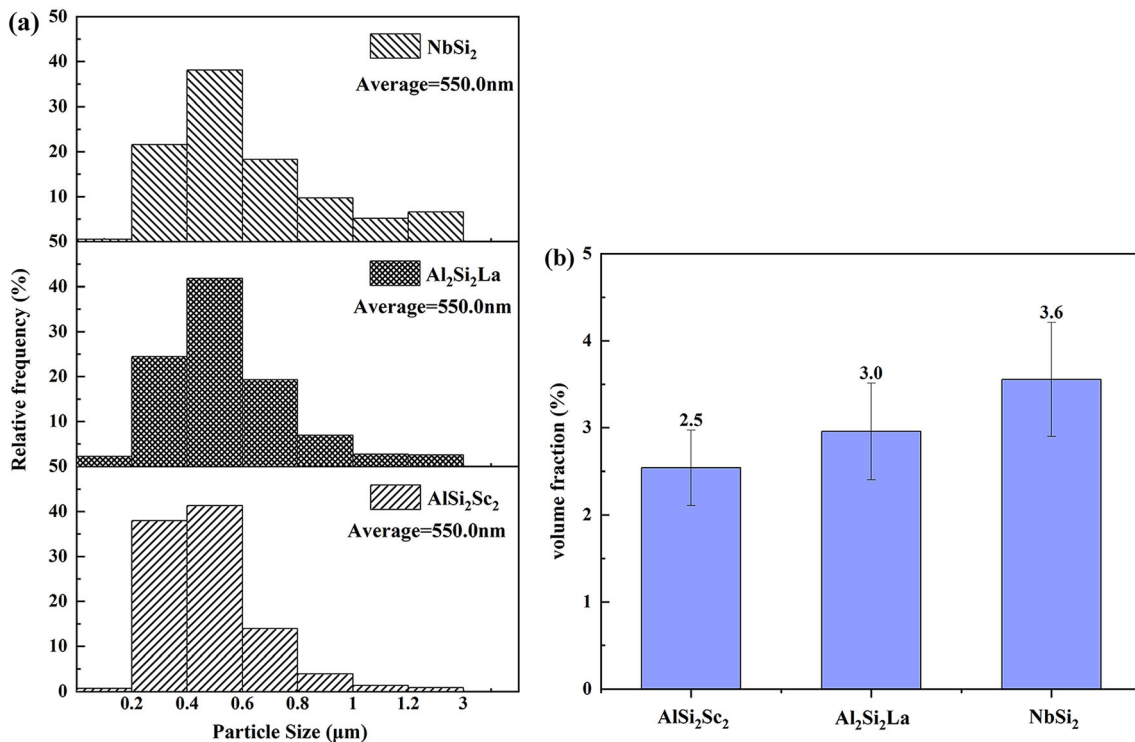

Fig. 12 Particle size distribution (**a**) and volume fraction (**b**) of the precipitates in Al–50Si–0.5X (X = Sc, La, Nb) alloys
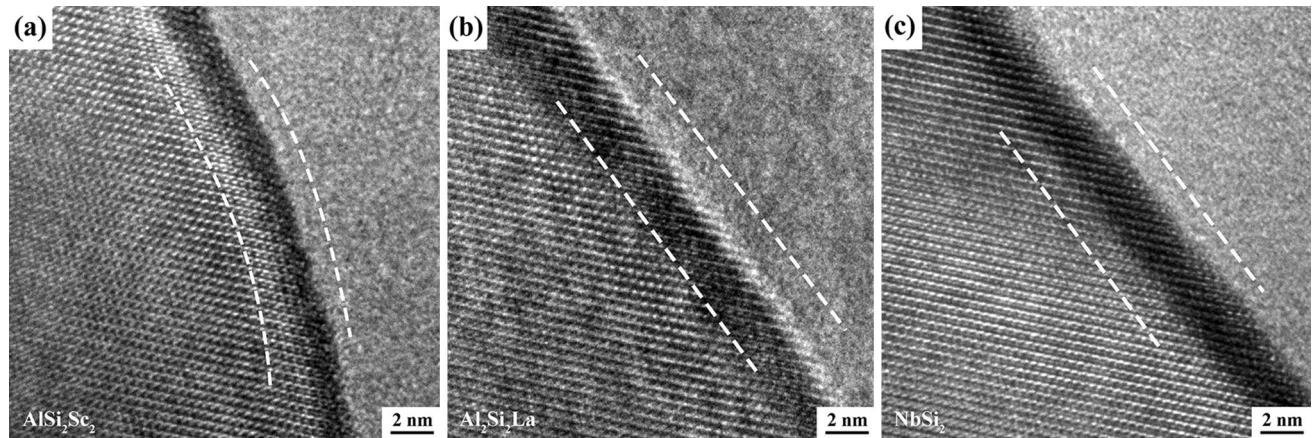
Fig. 13 High-resolution transmission electron microscopy (HRTEM) images of the **a** Al–50Si–0.5Sc, **b** Al–50Si–0.5La, **c** Al–50Si–0.5Nb alloys

20.7 MPa, and 23.4 MPa, respectively. Compared with the data in Table 2, the calculated values are consistent with the experimental results (21.3 MPa, 31.3 MPa, and 41.3 MPa, respectively). The deviation is mainly due to the slight difference in the morphology and content of Si, and some errors in the Image-Pro Plus (IPP) software statistics for the size and volume fraction of the precipitates. From Fig. 3, it is found that the alloying elements also affect the morphology of the connected Si phase. The size of the connected Si phase is relatively smaller in the Al–50Si–0.5Nb alloy, followed by the alloy containing La. The stress concentration of large size Si particles is more pronounced, and these Si particles tend to crack preferentially, leading to the decrease of tensile strength. The addition of alloying elements reduces the size of Si phase in the Al–50Si–0.5X (X = Sc, La, Nb) alloys, which slows down the stress concentration, and slightly improves the tensile strength of alloys.

5 Conclusions

(1) The addition of alloying elements Sc, La, and Nb has little effect on the size, distribution, and morphology of Si phase in the Al–50Si alloys prepared by gas atomization and hot pressing. In the alloys containing Sc, La, and Nb, the precipitates are $AlSi_2Sc_2$(V phase), Al_2Si_2La, and $NbSi_2$, respectively.

(2) The size distribution of $AlSi_2Sc_2$, Al_2Si_2La, and $NbSi_2$ precipitates is 0.2–3 μm, but most of them are concentrated in 400–600 nm, and the

average size is approximately 550.0 nm. The volume fraction of $AlSi_2Sc_2$, Al_2Si_2La, and $NbSi_2$ precipitates is 2.5%, 3.0%, and 3.6%, respectively.

(3) The precipitation strengthening plays a dominant role in the strength of Al–50Si–0.5X (X = Sc, La, Nb) alloys. Accordingly, the volume fraction of precipitates is the key factor in determining the alloy strength due to their similar particle size. Therefore, the Al–50Si–0.5Nb alloy has the highest tensile, flexural, compressive strength, and Brinell hardness, followed by the Al–50Si–0.5La and Al–50Si–0.5Sc alloys. However, the fracture and impact toughness decrease with the addition of alloying elements.

(4) The formation of precipitates increases the interfacial area and hinders the heat conduction, leading to the reduced thermal conductivity of the Al–50Si alloys with alloying elements. Moreover, the precipitates and Si phase jointly inhibit the thermal expansion of Al matrix, and the CTE of these alloys is slightly reduced.

Author contributions

All authors contributed to the study conception and design. Material preparation, data collection, and analysis were performed by JL and ZC. The first draft of the manuscript was written by JL and all authors commented on previous versions of the manuscript. All authors read and approved the final manuscript.

Funding

Declarations

Competing interest The authors declare no competing financial interests or personal relationships that could have influenced the work reported in this paper.

Availability of data and material Data transparency.

Code availability Software application or custom code.

References

1. J. Cho, K.E. Goodson, Nat. Mater. **14**(2), 136–137 (2015)
2. P.J. Ward, H.V. Atkinson, P.R.G. Anderson, L.G. Elias, B. Garcia, L. Kahlen, J.-M. Rodriguez-ibabe, Acta Mater. **44**(5), 1717–1727 (1996)
3. Y. Jia, F. Cao, S. Scudino, P. Ma, H. Li, L. Yu, J. Eckert, J. Sun, Mater. Des. **57**, 585–591 (2014)
4. A. Rodriguez-Guerrero, S.A. Sanchez, J. Narciso, E. Louis, F. Rodriguez-Reinoso, Acta Mater. **54**(7), 1821–1831 (2006)
5. Z. Cai, C. Zhang, R. Wang, C. Peng, K. Qiu, Y. Feng, Mater. Des. **87**, 996–1002 (2015)
6. N. Kang, P. Coddet, H. Liao, T. Baur, C. Coddet, Appl. Surf. Sci. **378**, 142–149 (2016)
7. Y. Li, J. Liu, W. Wang, G. Liu, Trans. Nonferrous Metals Soc. China. **23**(4), 970–976 (2013)
8. C. Cui, A. Schulz, K. Schimanski, H.W. Zoch, J. Mat. Process. Technol. **209**(11), 5220–5228 (2009)
9. K. Yu, S. Li, L. Chen, W. Zhao, P. Li, Trans. Nonferrous Metals Soc. China. **22**(6), 1412–1417 (2012)
10. Z. Cai, C. Zhang, R. Wang, C. Peng, X. Wu, H. Li, Mater. Sci. Eng. A. **730**, 57–65 (2018)
11. J. Fang, Y. Zhong, M. Xia, F. Zhang, Trans. Nonferrous Metals Soc. China. **31**(3), 586–594 (2021)
12. C. Xu, W. Xiao, S. Hanada, H. Yamagata, C. Ma, Mater. Char. **110**, 160–169 (2015)
13. Y. Tzeng, S. Jian, Mater. Sci. Eng. A. **723**, 22–28 (2018)
14. X. Wu, H. Zhang, H. Jiang, Z. Mi, H. Zhang, Metals. **10**(5), 621 (2020)
15. M. Nowak, L. Bolzoni, N.H. Babu, Mater. Des. **66**, 366–375 (2015)
16. L. Bolzoni, M. Nowak, N.H. Babu, Mater. Des. **66**, 376–383 (2015)
17. M.F. Kilicaslan, W. Lee, T. Lee, Y. Sohn, S. Hong, Mater. Lett. **71**, 164–167 (2012)
18. N. Raghukiran, R. Kumar, Mater. Sci. Eng. A. **641**, 138–147 (2015)
19. J. Dumbre, S.K. Kairy, E. Anber, T. Langan, M.L. Taheri, T. Dorin, N. Birbilis, J. Alloys Compd. **861**, 158511 (2021)
20. J.Y. Chang, G.H. Kim, I.G. Moon, C.S. Choi, Scr. Mater. **39**(3), 307–314 (1998)
21. J.C. Zhao, L.A. Peluso, M.R. Jackson, L.Z. Tan, J. Alloys Compd. **360**(1–2), 183–188 (2003)
22. Y. Li, B. Hu, Q.F. Gu, B. Liu, Q. Li, Scr. Mater. **160**, 75–80 (2019)
23. F. Zhang, A. Qin, S. Liu, J. Wang, Y. Du, J. Mater. Sci. **51**(3), 1644–1658 (2016)
24. A. Rezaei, H.R.M. Hosseini, Mater. Sci. Eng. A **771**, 138573 (2020)
25. Y.Q. Liu, S.H. Wei, J.Z. Fan, Z.L. Ma, T. Zuo, Mater. Sci. Technol. **30**(4), 417–422 (2014)
26. O. Elsebaie, A.M. Samuel, F.H. Samuel, J. Mater. Sci. **46**(9), 3027–3045 (2011)
27. O. Elsebaie, A.M.A. Mohamed, A.M. Samuel, F.H. Samuel, A.M.A. Al-Ahmari, Mater. Des. **32**(6), 3205–3220 (2011)
28. D. Chen, C. Xia, Z. Chen, Y. Wu, M. Wang, N. Ma, H. Wang, Mater. Lett. **138**, 148–150 (2015)
29. E.M. Elgallad, M.F. Ibrahim, H.W. Doty, F.H. Samuel, Philos. Mag. **98**(15), 1337–1359 (2018)
30. J. Du, H. Tu, H. Peng, Y. Liu, C. Wu, J. Wang, X. Su, J. Alloys Compd. **765**, 608–615 (2018)

31. A.M. Cardinale, D. Macciò, G. Luciano, E. Canepa, P. Traverso, J. Alloys Compd. **695**, 2180–2189 (2017)

32. D. Turnbull, B. Vonnegut, Ind. Eng. Chem. **44**(6), 1292–1298 (1952)

33. S. Queyreau, G. Monnet, B. Devincre, Acta Mater. **58**(17), 5586–5595 (2010)

34. M.J. Starink, S.C. Wang, Acta Mater. **51**(17), 5131–5150 (2003)